Ocean Sci. Discuss., 9, 2081–2120, 2012
www.ocean-sci-discuss.net/9/2081/2012/
doi:10.5194/osd-9-2081-2012

Ocean Science Discussions

Ocean state indicators from MyOcean altimeter products

L. Bessières[1], M. H. Rio[2], C. Dufau[2], C. Boone[2], and M. I. Pujol[2]

[1]AS+ – EOLEN, 5 avenue Didier Daurat, 31400 Toulouse, France
[2]CLS-DOS 8-10 rue Hermès – Parc Technologique du canal-31250 Ramonville Saint Agne, France

Received: 1 March 2012 – Accepted: 2 April 2012 – Published: 24 May 2012

Correspondence to: L. Bessières (laurent.bessieres@cls.fr)

Published by Copernicus Publications on behalf of the European Geosciences Union.

Abstract

The Sea Level Thematic Assembly Center from the MyOcean project provides observations of the ocean dynamic topography from altimeter measurements. Three specific indicators have been developed, based on altimeter data only, in order to monitor the ocean state. The first ocean indicator observes the positive and negative phases of the ENSO events in the Tropical Pacific, the El Niño/La Niña events since 1992. The second ocean indicator checks the contracted or extended state of the Kuroshio Extension. The last ocean indicator is dedicated to the Ionian basin in the Mediterranean Sea and permits to separate "zonal-cyclonic" state (1998–2005 and since 2011 up to now) from the "anticyclonic" state (1993–1996) usually discussed in the literature. In addition it allows identifying a third state in which both the anticyclonic circulation around the northern part of the basin and the strong zonal Mid-Ionian jet co-exist (2008–2010). Besides providing useful indices to monitor the ocean state, these indicators are a new tool to assess the long-term quality of the SLTAC products.

1 Introduction

The Sea Level Thematic Assembly Center (SLTAC) of the MyOcean project (http://www.myocean.eu.org/) is dedicated to the production of Sea Level information from altimeter measurements. Together with the other TACs (dedicated to Ocean Color, Sea Surface Temperature, Sea Ice, Wind and In-Situ data) and the Monitoring and Forecasting Centers (MFCs), one of its missions is to develop ocean state indicators (also called specific core products) for the European Environmental Agency (EEA) to measure and report on the overall behavior of the global ocean and European sea in a cost-effective and meaningful way. Ocean state indicators are a simple representation of ocean-climate variability that provides an at-a-glance overview of the state of the ocean climate and help track trends over time and between places. They also are a

OSD
9, 2081–2120, 2012

way to talk to a wider audience about the ocean observing system as they monitor phenomena with a potentially high significant social impact.

Several ocean state indicators already exist, based on observational analyses sourced from different operational centers and updated on a weekly or monthly basis, like the Global mean sea level and global mean sea surface temperature, the Bermuda-Labrador Basin Transport Index, the Tropical Northern Atlantic Index, the Oceanic Niño Index or Niño3.4 SSTA, the Southern Oscillation Index or the Western Tropical Indian Ocean (WTIO) index. The OOPC (Ocean Observations Panel for Climate)/UNESCO website (http://ioc-goos-oopc.org/state_of_the_ocean/all/) gives more details on each existing index.

By providing globally and continuously a large amount of sea surface height measurements, satellite altimetry is a key component of the global ocean observations system. The Sea Surface Height observed by satellite altimetry is therefore a relevant tool to monitor the evolution of the ocean variability. Since several years, the Global Mean Sea level trends indicators generated by the LEGOS/CNES/CLS team (ref) is regularly provided to intergovernmental bodies as OOPC, CEOS (http://idn/ceos.org/climdiag/). A specific work has also been performed for EEA in order to provide European seas regional mean sea level trends for the EEA State of environment report (EEA, SOER 2010). In this paper, we used the altimeter products provided by the DUACS system (Dibarboure et al., 2011) operated by the SLTAC to build three additional ocean indicators of well-known oceanic phenomena, i.e. the ENSO events, the contracted/extended state of the Kuroshio Extension and the reversal of the surface circulation in the central part of the Mediterranean Sea (Ionian Basin). In order to provide highest quality products, the SLTAC/DUACS altimeter data processing engine is intricately linked with calibration and validation activities. In addition to providing a useful tool to follow the evolution of the ocean state, the development of ocean indicators and their long-term monitoring represent an innovative approach to assess the quality of the SLTAC/DUACS altimeter products.

OSD
9, 2081–2120, 2012

Section 2 details the data and methods used to define these new indicators. Sections 3, 4 and 5 describe respectively the El Niño indicator, the Kuroshio Extension indicator and the Ionian Surface Circulation indicator. Conclusion and perspectives are finally given in Sect. 6.

2 Data and methods

2.1 The SLTAC products

The SLTAC products are obtained from the Level 2 altimeter products (i.e. Geophysical Data Record GDR), available under three forms: fast delivery product and Intermediate product, both used in operational processing, and Delayed Time product involved in reprocessing. Although each altimeter mission is processed separately a consistency between the different missions is ensured by a homogenization process that consists in applying the most recent corrections, models and references recommended by agencies or expert groups. The up-to-date list of corrections and standards are given in the SSALTO/DUACS users' handbook (2011). In addition, a multi-mission cross-calibration processing is applied to ensure consistency and accuracy of all the data flows from all satellites. Empirical processes are used to minimize long-wave geographically correlated errors. First, a two step orbit error reduction is applied using crossover minimization with a reference mission. Then, a second cross-calibration process is applied to reduce residual long-wavelength error signal. Once altimeter data have been validated and inter-calibrated, different Sea Level Anomaly (SLA) products are generated using a reference sea surface corresponding to the 1993–1999 period. Data are first projected onto theoretical co-located track positions, using precise cross-track projection and interpolation schemes. A final quality control processing is applied on these data to edit possible isolated and slightly erroneous measurements. Finally information from the different altimeters is merged through an optimal interpolation to produce gridded SLA fields (Ducet et al., 2000).

OSD
9, 2081–2120, 2012

The ocean variability can be studied directly from these maps of SLA (MSLA) or by differentiating them into Eddy Kinetic Energy (EKE) trough the geostrophic approximation formulae (Eq. 1).

$$\mathrm{EKE} = \frac{1}{2}(u_g'^2 + v_g'^2) \quad \text{with} \quad u_g' = -\frac{g}{f}\frac{\partial \mathrm{SLA}}{\partial y} \quad \text{and} \quad v_g' = +\frac{g}{f}\frac{\partial \mathrm{SLA}}{\partial x} \tag{1}$$

where g is the gravity and f the Coriolis coefficient.

Maps of Absolute Dynamic Topography (MADT) will also be used in the following to analyze surface circulation patterns. The MADT are obtained by adding the Mean Dynamic Topography (MDT) to the MSLA (Eq. 2).

$$\mathrm{MADT} = \mathrm{MSLA} + \mathrm{MDT} \tag{2}$$

The MDT used in Sect. 3 is the CNES-CLS09 MDT (Rio et al., 2011) whereas the MDT used in Sect. 4 is a regional MDT (Rio et al., 2007) dedicated to the Mediterranean Sea. Both of them are computed using a combination of in-situ data (surface drifting buoys, ARGO floats, CTD and XBT casts) and altimeter data.

The SLTAC center produces global 1/4° gridded maps of the global ocean as well as 1/8° gridded maps for regional seas as the Mediterranean Sea, the Black Sea and the Arctic Sea. Both Near Real Time (NRT) and Delayed Time (DT) maps are available. The ocean indicators described in this paper were developed using both DT and NRT products when available.

2.2 EOF decomposition analysis

The joint space and time dependency of the ocean variability makes its analysis difficult. In order to decouple these two dimensions a Empirical Orthogonal Functions (EOFs) decomposition analysis is used (see e.g. Toumazou and Cretaux (2001) for a classical use of EOFs in ocean research). This method allows decomposing such a time and space dependant signal into a sum of principal components. Each component is made of an eigenvalue (λ) and an eigenvector (also called EOF) of the covariance

OSD
9, 2081–2120, 2012

matrix. For each mode, the eigenvalue gives the relative contribution of the mode with respect to the full signal whereas the eigenvector shows the spatial distribution of the variable associated to a time series, called Principal Component (PC) Time Series. The geophysical signal $S(x,y,t)$ can hence be written as:

$$S(x,y,t) = \sum_{1}^{N} \lambda_i \mathrm{EOF}_i(x,y)\mathrm{PC}_i(t) \quad (3)$$

The decomposition of MSLA or EKE signal into EOFs is a powerful mean to ease the ocean variability analysis and the determination of ocean state indicators. It will be used in Sects. 4 and 5 to better define the altimetry-based ocean indicators.

3 Monitoring the El Niño Southern Oscillation (ENSO)

3.1 Description of ENSO events

For centuries, Peruvian fishermen have feared the sea warming event called "El Niño" which, every few years, around Christmas, drastically reduces their fishing catches. These El Niño events belong to a broader disruption of normal weather patterns which causes drought, flooding and hurricanes around the world. In the tropical Pacific, ocean and atmosphere circulations are closely linked, each reacting quickly to changes in the other.

In normal conditions, easterly trade winds push surface Pacific waters towards Australia and the Philippines, creating a warm pool at the western end of the basin with higher temperatures and sea level. Over the ocean, these winds load up with moisture and release it as heavy rains over the warm pool. Meanwhile, at the eastern end of the basin, nutrient-rich cold waters upwell to the surface, favorable for anchovy which abounds along the Peruvian coast.

During an "El Niño" situation, westerly wind bursts at the western end of the basin and the warm pool drifts eastward into the central Pacific. The trade winds weaken and

OSD
9, 2081–2120, 2012

the storm zone moves eastward with the warm pool. Heavy rainfall floods coastal areas of western South America. The thermocline deepens and there is no longer upwelling of cold and nutrient-rich water off the coasts of Chile and Peru. The surface waters are warmer and fish stocks dwindle.

During "La Niña", which is somewhat the opposite of "El Niño", the trade-winds strengthen, shrinking the warm pool and cooling the Tropical Pacific. The climate becomes drier and colder off the coast of America. Rain is abundant over Indonesia and upwelling of cold water is more intense along the west coast of South America leading to abundance of anchovy.

3.2 ENSO analysis with sea surface temperature

As the ocean state linked to ENSO causes strong social and economical damages, several monitoring of the Tropical Pacific have been already established (e.g the TOGA/TRITON moored buoy array). UNESCO calculates weekly the Oceanic Niño Index (ONI) with the Reynolds OIv2 (Reynolds et al., 2002) Sea Surface Temperature (SST) analysis, made available through the International Research Institute Data Library. The anomaly is calculated relative to a climatological seasonal cycle based on the years 1982–2005. In the same purpose, the National Oceanic and Atmospheric Administration (NOAA) analyses three month running means of Extended Reconstructed SST (ERSST.v2) anomalies (Smith et al., 2004) in the Niño 3.4 region (5° N–5° S, 120–170° W). Episodes are identified using an ONI threshold of ±0.5 °C, based on the 1971–2000 period. For historical purposes, cold and warm episodes are defined when the threshold is met for a minimum of 5 consecutive overlapping seasons. Thus so far, the Sea Surface Temperature is the main variable used to monitor El Niño, in particular in the Niño3.4 area.

OSD
9, 2081–2120, 2012

3.3 The altimetry-based El Niño Ocean indicator

Altimetry is also a good candidate for providing information on El Niño using sea level anomaly (SLA). In order to compute an altimetric indicator for the El Niño/La Niña events, we first extracted the Niño3.4 area from the 1/3° global altimeter maps. The Delayed Time (DT) is used when available since it is the best altimeter dataset. For more recent time, Near Real Time (NRT) products are used, which quality is slightly lower. In order to focus on the inter-annual signal, the bi-annual and annual cycles are removed from the data. Furthermore, a 60 days period is also removed in the altimeter products due to aliasing of tides, orbit and radiometer at the nearly 10 days repeat cycle from TOPEX and JASON. As this signal is not geophysical, it is removed even though it is very small. As mentioned earlier, the SLA delivered by the SLTAC are referenced to a 7 yr time period (1993–1999). This is short compared to the SST availability period. We tested the impact of the reference period length on the results by using either a 7 or 14 yr reference period. Similar indexes were obtained in both cases (not shown here). For better statistical representation, we set the reference period to the longest period currently available, i.e. 18 yr (1993–2010). The SLA are thus calculated with respect to this mean. The index is built by dividing the SLA by the standard deviation (computed over the same reference period) and then averaging the values in the Niño3.4 area. An analysis is performed every week, the output time series is smoothed over 3 months to filter out high variability. The resulting time series is shown Fig. 1. It is currently published weekly on the AVISO website.

We validate the obtained Niño index by applying the same process to Reynolds SSTs. The three indices NOAA ONI (1971–2000 based period), SST (1993–2006 based period) and SLA (1993–2006 based period) are very close to each other (Fig. 2). The comparison NOAA ONI with SST mainly shows the impact of the reference period on the index and the two collocated time series show a good 0.99 correlation. The SLA index compares well with the NOAA ONI (correlation of 0.88) and the SST index

OSD
9, 2081–2120, 2012

(correlation of 0.89). We conclude that the SLA index is an indicator of an el Niño/la Niña event as precise as the SST based indicator (Fig. 1).

4 Monitoring the Kuroshio Extension (KE)

4.1 The Kuroshio Extension

The Kuroshio Extension (KE) is an eastward-flowing inertial jet in the subtropical western North Pacific after the Kuroshio separates from the coast of Japan at 35° N, 140° E. Being the extension of a wind-driven western boundary current, the KE has long been recognized as a current system rich in large-amplitude meanders and energetic pinched-off eddies. The KE region has the largest sea-surface height variability on sub-annual and decadal time scales in the extratropical North Pacific Ocean (Qiu, 2002). The decadal variability is related to transitions of the KE from a highly energetic elongated path to a weaker contracted and more convoluted path (Qiu and Chen, 2005). Prediction and monitoring of the path of the Kuroshio is of huge importance for local fisheries and hence local economies (Kagimoto et al., 2008) as the position of the Kuroshio strongly determines the regions where phytoplankton and hence fish are located. The KE variability has been studied by numerous experimental studies, like WESTPAC at 152° E, the Kuroshio Extension Region Experiment (KERE) at 143° E or the Kuroshio Extension System Study (KESS) at 146° E as well as by numerical studies (Kramer et al., 2011). Here, the long time series of delayed time Sea Level TAC products are used to investigate the low-frequency changes of the Kuroshio Extension (KE) jet.

4.2 KE analysis with sea level

The dominant low-frequency signal of the KE over the last seventeen years is characterized by a modulation of its zonal mean flow intensity. This modulation results in

OSD
9, 2081–2120, 2012

two rather different states of the KE: an "elongated state" (also called "strong state") corresponding to a narrow strong steady jet (top right panel of Fig. 3), and a "contracted state" (also called "weak state") in which the jet is weaker and more unsteady, spreading on a wider latitudinal band (top left panel of Fig. 3). During elongated time period, two quasi-stationary meanders are well-developed with their ridges located at 144° and 150° E respectively (top and bottom right panel of Fig. 3), while they are barely discernible during contracted phases (top and bottom left panel of Fig. 3). South of the quasi-stationary meanders, the KE jet is flanked by a tight recirculation gyre whose circulation increases the eastward transport of the KE from the local Sverdrup transport (bottom right panel of Fig. 3). Between these two main states the KE jet has many intermediate states of transition and presents either progressively weakning or strengthening trends. The weakning (strengthening) of the zonal mean flow intensity can be connected with westward expansions of wind-induced Sea Level Anomalies propagating by baroclinic Rossby waves (Qiu and Chen, 2005). These Sea Level Anomalies are generated at mid-latitudes in the eastern North Pacific by wind stress curl anomalies during the different phases of the Pacific Decadal Oscillation (PDO) (Qiu, 2003). Yet, El-Niño Southern Oscillation (ENSO) also generates low-latitudes SSH anomalies that can be propagated northward at mid-latitudes via western boundary currents and hence have a significant impact on the resulting SSH level of the KE region (Qiu and Lukas, 1996). The dominant interannual to decadal variability of the KE region is therefore connected with the two main large-scale circulation oscillation of the Pacific: the PDO and the ENSO, with possible complex coupled interactions.

4.3 The KE altimetry-based indicator

When the KE jet is in a weaker (resp. stronger) state, the upstream KE path tends to become more (resp. less) variable and regional eddy kinetic energy level tends to be higher (resp. lower) (Fig. 4). Yet this former relationship is rather counterintuitive since jet stability analysis usually suggests that stronger mean flows favor baroclinic instabilities and lead to more mesoscale activities. This clearly indicates that baroclinic

OSD
9, 2081–2120, 2012

instability is not the dominant mechanism controlling the variability of the mesoscale eddy field in the KE region. This plurality and variability of EKE energy sources suggest that the definition of an oceanic indicator of the Kuroshio jet state is not trivial. A way of caracterizing the dynamics of the region and its variability is to decompose the high-frequency EKE (HF-EKE) into empirical orthogonal functions (Fig. 5). Following Brachet (2005), the HF-EKE is derived from the 200-days high pass filtered SLA in order to extract the mesoscale from the lower-frequency signals. The HF-EKE is then centered and filtered with a 13-months moving average so as to remove the seasonal signal. The remaining variability modes are interannual-to-interdecadal modes. During the period 1993–2011, the first mode of the HF-EKE EOF decomposition accounts for 30 % of the total variance. It exhibits a longitudinal spatial distribution of the signal both upstream (141–153° E) and downstream (153–165° E) the KE jet, with a strong zonal gradient leading to a sign reversal about 150–155° E (top panel of Fig. 5). Combined with sign reversals of its temporal component (bottom panel of Fig. 5), this zonal out of phase in the spatial distribution of the variance generates a longitudinal bi-polarity associated with the two opposite states of the KE jet (elongated vs. contracted). The maximum intensities are located upstream in the western part of the KE in the center of the positive cell.

To stick to the El Nino indicator definition strategy, we have tried to define an oceanic indicator based on a mean boxed EKE .The square box: B1 = (142–149° E, 32–37° N) was found to catch most of the positive pattern when averaging the HF-EKE (Fig. 5). The temporal evolution of the mean standardized HF-EKE defined in box B1 during the period 1993–30 November 2011 (Fig. 6) shows similar variations to those obtained for the mode 1-temporal component in the HF-EKE EOF decomposition method (bottom panel of Fig. 5). Blue shaded areas correspond to elongated states periods (1993–94, 2002–04 and 2010–11), while orange shaded areas fit contracted states periods (1997–2001 and 2009). For each year of the orange and blue shaded periods the yearly path (as defined in Fig. 6, two top panels) always matches one of the two patterns of Fig. 5. Between these two opposite phases the KE jet has many intermediate states

OSD
9, 2081–2120, 2012

of transition and presents either progressively weakning (1994–97 and 2004–2009) or strengthening (2001–2002 and 2009–2010) trends.

5 Monitoring the surface circulation in the Ionian Basin, Mediterranean Sea

5.1 Decadal oscillations of the Ionian surface circulation (IoSC)

Several experimental and numerical studies have documented the Ionian upper layer circulation (e.g. Pinardi et al., 1997; Pujol and Larnicol, 2005; Hamad et al., 2005; Gačić et al., 2011). These works reveal that the dominant low-frequency dynamic of the Ionian Sea over the last twenty years is characterized by a decadal oscillation of its upper layer basin-wide circulation. This modulation results in two rather different states of the IoSC associated with a circulation reversal in the Northern part of the Ionian Sea reversing from a cyclonic mode (also called zonal mode) to an anticyclonic mode and vice versa. The "anticyclonic state" corresponds to the presence of an anticyclonic gyre in the northern part of the Ionian basin (namely anticyclonic North Ionian Gyre (NIG)) and is associated with a weak quasi-zonal jet crossing the Ionian Sea from west to east (namely the Mid-Ionian Jet (MIJ)) (top right panel of Fig. 9). Conversely, the "cyclonic state" is related to a reversal of the NIG (cyclonic NIG) and is associated with an intense MIJ (bottom right panel of Fig. 9). The Ionian interior is the crossroads of transiting waters connecting the Western and the Eastern Mediterranean basins with the Adriatic and the Aegean Seas. During anticyclonic time period, the Atlantic Ionian Stream (AIS) entering the Sicily Strait bifurcates almost exclusively northeastward in the Ionian where it meanders anticyclonically bringing Modified Atlantic Waters (MAW) into the Ionian interior and eventually into the Adriatic before reaching the Levantine basin via the Cretan passage. In contrast, during zonal phases the AIS is prolonged eastward by an intense MIJ, what conveys MAW directly from the Sicily Strait to the Cretan Passage and the Levantine basin by the shortest route. Under cyclonic mode, the cyclonic-zonal circulation pattern contributes to make the eastern Mediterranean

OSD
9, 2081–2120, 2012

(EMed) waters more prone to spread westward into the Ionian interior with possible incursion into the Adriatic. Between these two main states the IoSC has many intermediate states of transition and presents either progressively weakening or strengthening trends.

The mechanisms of origin of those decadal oscillations have been discussed in a few studies. In 1997 the surface circulation of the Northern Ionian basin reversed from anticyclonic to cyclonic and Larnicol et al. (2002) suggested that the renewal of deep and intermediate water masses in the Eastern basin, as discussed by Klein et al. (1999), is likely to have a signature on sea surface heights through density variations. Vigo et al. (2005) assumed that such density variations are able to sustain surface circulation reversal in the Ionian. During the 1990s, the Southern Adriatic area of deep water formation switched to the Cretan Sea. This transition is called the Eastern Mediterranean Transient (EMT) and is followed by a massive dense-water output of Cretan Sea Outflow Water (CSOW) from the Aegean Sea. Roether et al. (2007) showed that such a massive outflow could generate changes not only in the deep layers but over the entire water column. According to Borzelli et al. (2009), the Ionian surface circulation reversal of 1997 took place in the presence of an anticyclonic wind field, therefore it could not be sustained by wind stress. Instead, the authors proposed that it was associated with a vorticity transfer due to the filling up of the Ionian bottom layer with the CSOW following the EMT. Before 1997, the CSOW mainly occupied the northeastern flanks of the Ionian with a decreasing concentration moving westward (Roether et al., 2007). This resulted in a bottom pressure gradient directed towards the center of the basin, which is able to sustain a stationary cyclonic shear in the bottom layer. The consequent upward displacement of the Ionian deep water led to a raising of isopycnes by several hundred meters (Klein et al., 1999) capable to generate an anticyclonic shear in the upper layer. Conversely, after 1997 the outflowing Adriatic dense water set up a bottom pressure gradient directed from the center of the basin toward the coasts, as its density is lower than the one of abyssal waters. This pressure gradient was able to sustain a stationary anticyclonic shear in the bottom layer and a cyclonic one in the

OSD
9, 2081–2120, 2012

upper layer. Therefore, according to Borzelli et al. (2009) the reversal from an anticyclonic to a cyclonic pattern of surface circulation can be the result of the inversion of the bottom pressure gradient. Comparing the rate of change of the ocean vorticity and the source of vorticity due to the wind stress Gačić et al. (2010) argue that variations in the upper Ionian circulation are effectively driven by internal oceanic processes, which can outweigh wind stress. These processes are proposed to be the result of a feedback mechanism (namely the Adriatic-Ionian Bimodal Oscillation System (BiOS)) between: (i) the redistribution of water masses, owing to variations in the thermohaline properties of the Southern Adriatic, and its consequent transfer of baroclinic vorticity and (ii) inversions of the upper Ionian circulation leading to possible alternate advection into the Adriatic of either saltier water from the Aegean-Levantine basin or fresher water of Atlantic origin (Gačić et al., 2011). Therefore the vorticity modifications are capable to sustain the reversals of the upper layer circulation, which in return are responsible of the variations in the thermohaline properties.

In the following sections, nineteen years of SLTAC/DUACS altimeter data have been used to investigate the low-frequency changes in the Ionian general surface circulation, in ordrer to define an efficient oceanic indicator of the different IoSC phases.

The definition of such an indicator – a question that has not been adressed yet in the litterature – is confronted to the same difficulties as the comprehension of the general circulation in the basin, i.e. the plurality of the mecanisms brought into play and their possible interactions and feedback mechanisms on decadal time scales (see previous subsection). Its determination is also made delicate since different types of circulations occur in opposite part of the basin: quasi-zonal jet circulation in the central and southern part of the basin versus cyclonic-anticyclonic gyre circulations in the northern part.

5.2 Ionian surface circulation analysis with sea level

As for the determination of the oceanic indicator of the Kuroshio jet state, we applied an EOF decomposition analysis on the altimeter signal. Yet, as shown by a qualitative

OSD
9, 2081–2120, 2012

comparison between top-left and bottom-left panels of Fig. 9, the choice of the SLA as a tracer of the northern IoSC inversions seems to be a more appropriate choice than an EKE based tracer. According to Pujol (2006), the SLA variability associated with the reversals of the northern IoSC is taken into account by the second variability mode during the period 1993–2003 and explains 5, 6 % of the total variance in the whole Mediterranean Sea, while the first variability mode, that explains 68 % of the total variance, is related to the seasonal variability including steric effects. For each mode, spatial patterns of variability and the associated temporal variations computed for the period 1993–2003 have been first reproduced for comparison purpose (not shown). Thereafter, in order to remove the seasonal signal and concentrate on interannual-to-interdecadal modes, the SLA has been filtered with a 13-months moving average. During the period 1993–2011, the mode 2 of the SLA decomposition accounts for 14.0 % of the total variance in the Mediterranean Sea (top panel of Fig. 10), while the most energetic first mode is responsible for 47 % of the total variance (not shown). The temporal and spatial characteristics of mode 1 are in agreement with trends characteristics found by Criado-Aldeanueva et al. (2008) for the period 1992–2005 and by Vigo et al. (2011) for the period 1992–2008. Therefore, the first mode is related to non-seasonal steric and mass-induced contribution, i.e. the non-seasonal component of the trend. The spatial structure of mode 2 is characterized by a high-amplitude circular pattern in the northwestern part of the Ionian (top panel on Fig. 10). The temporal variations of its amplitude reveal prevalently decadal variability (bottom panel on Fig. 10). The high-amplitude circular feature of mode 2 coincides with the cyclonic-anticyclonic NIG circulation pattern as evidenced from the yearly average ADT current fields (Fig. 16). Therefore, the inversions of the NIG are associated with sign reversals of the temporal component in mode 2. Figure 10 shows that the temporal locations of the NIG inversion is in good agreement with what is expected for the cyclonic-anticyclonic inversion at the end of year 2005, while the anticyclonic-cyclonic inversion of year 1997 occurs later in 1998. Moreover, unlike what can be observed on Fig. 16 for year 1994, the anticyclonic circulation pattern is missing on Fig. 10. A more precise view can be obtained

OSD
9, 2081–2120, 2012

using a square box: S1 = (15–20° E, 35–40° N) (see its location on Fig. 10) in order to catch most of the northwestern circular pattern when averaging the SLA. The temporal evolution of the mean SLA defined in box S1 during the period 1993–2011 is shown on Fig. 10.

At first order, its variations are similar to those obtained with the temporal component of the second EOF mode of SLA. Furthermore, the North Ionian focused box average method enables to fit the anticyclonic period of 1993–1996 and its inversion toward cyclonic period with what is observed on yearly average ADT fields (Fig. 16).

Concerning the cyclonic period of 1998–2005, note that in spite of similar amplitudes of mean boxed SLA in both phases of the NIG, maps of ADT with overlaid total velociy fields reveals an asymmetry in the velocity intensities according to the phase of the NIG. The mean total velocity modulus defined in box S1 during the period 1993–2011 reveals significantly higher intensities during anticyclonic NIG O ($5\,cm\,s^{-1}$) than during cyclonic NIG O ($0.8\,cm\,s^{-1}$). Thus, as confirmed by the yearly average ADT fields (Fig. 16) the surface signature of the cyclonic NIG may be almost unnoticeable during cyclonic period, what is problematic for an oceanic indicator based on surface remote sensing. Yet, as observed by Pujol and Larnicol (2005), the intensity of the MIJ increases during the cyclonic period after 1997. This predominance of the MIJ compared to the cyclonic NIG, can be observed on the yearly average ADT fields during the period 1998–2005 (Fig. 16). It must be noticed that though possible, an overestimation of the MIJ in the MDT field remains weak since: (i) unlike near the coasts, data sampling make it possible to correctly detect the stream in the central part of the basin, (ii) altimetric errors in that part of the basin are weaker than close to the coasts, (iii) the spatial distribution of the low-frequency EKE (i.e. derived from the 100-days low pass filtered SLA) in the yearly and monthly average fields (not shown) is consistent with the existence of an intense MIJ, and (iv) using drifters Gerin et al. (2009) have shown that the main feature for year 2005 is an eastward flow entering the Sicily Strait and crossing the Ionian in its central part. That is why in term of surface circulation, talking about “cyclonic-zonal” state instead of a fully “cyclonic” state seems to be justified.

OSD
9, 2081–2120, 2012

Besides the two main patterns of circulation (fully anticyclonic and cyclonic-zonal), a mixed state is also possible in which the anticyclonic NIG coexist with the zonal MIJ as during year 2007 (right panel of Fig. 12). Contrary to year 1997, this state is not a temporary transition since it lasts 4, 5 yr from the cyclonic-anticyclonic inversion of the end of year 2005 to the middle of year 2010.

As for the cyclonic year 1998 (bottom-middle panel of Fig. 9), the MIJ signature is noticeable in the spatial distribution of the 2007 yearly averaged LF-EKE (middle panel of Fig. 12). Yet, unlike for years 1995 and 1998, the spatial distribution of the 2007 yearly averaged SLA does not present a latitudinal bi-polarity associated with the northern and the southern part of the Ionian. Instead, the spatial distribution of the SLA for year 2007 is basically different since alternate mesoscale SLA structures fill the whole basin (left panel of Fig. 12). These discrepancies (resp. similarities) concerning the SLA (resp. LF-EKE) can be generalized for all years over the period 2006–2010 when compared with all years of either the anticyclonic period of 1993–1996 or the ones of the cyclonic period 1998–2005 (not shown), what tends to prove that the circulation pattern observed during the period 2006–2010 is related to a third "Anticyclonic-Zonal" state of the IoSC. Therefore, an oceanic indicator that would be only based on mean boxed SLA would not be able to discriminate fully "Anticyclonic" state period (e.g. 1993–1996) from "Anticyclonic-Zonal" state period (e.g. 2006–2010).

5.3 Ionian surface circulation analysis with EKE

The presence/absence of the MIJ distinguishes fully "Anticyclonic" from "Anticyclonic-Zonal" state period (Fig. 16). The SLA signature of the MIJ is weak (bottom left panel of Fig. 9 and top panel of Fig. 10), however as jets are likely to generate intense SLA gradients, their surface signature should be seen in the EKE field. The total EKE decomposition in HF-EKE and low-frequency EKE (LF-EKE) has been deduced, respectively, from the low- and the high-frequency component of the SLA, both computed applying a Loess low-pass time filter to the SLA signal in order to extract a signal higher and lower than 100 days. As underlined by Pujol and Larnicol (2005), LF-EKE clearly evidences

OSD
9, 2081–2120, 2012

the variability of the intensity of the MIJ, while HF-EKE rather traduces the measoscale activity linked to the MIJ. In the following, we thus focus on the LF-EKE component. Following Brachet (2005), the LF-EKE is then centered and filtered with a 13-months moving average so as to remove the seasonal signal. Therefore remaining variability modes are interannual-to-interdecadal modes.

During the period 1993–2011, the mode 1 of the LF-EKE EOF decomposition accounts for about 12 % of the total variance in the Ionian basin. Top panel of Fig. 5 shows a quasi-zonal spatial distribution of the signal crossing the central part of the Ionian from the Sicily Strait to the Cretan Passage and associated with the MIJ trajectory. The meridional spreading of the pattern (about 4° of latitude at 17° E) is related to the intense MIJ low-frequency dynamics and instabilities subsequently responsible for the intense mesoscale variability in that part of the basin (Hamad et al., 2005). Therefore, weak LF-EKE intensities correspond to the absence or to a weak activity of the MIJ, while strong LF-EKE intensities are the signature of a strong activity of the MIJ. The level corresponding to −0.9 has been indicated on Fig. 5 in order to link phases of weak/strong LF-EKE intensities with respect to the absence/presence of the MIJ respectively (Fig. 16).

As for the mean boxed SLA, the possibility to obtain a more precise view has been tested by using square boxes for average. Numerous sensibility tests have been done concerning the boxes location in order to catch the highest level of variability and to accentuate previous evidenced states of the IoSC. Location of retained boxes is mentioned on top panel of Fig. 5: E1 = [11–14° E, 36–37° N], E2 = [17–18.5° E, 35.5–36.5° N], E3 = [15–18.5° E, 34.5–35.5° N], E4 = [16–19.5° E, 33–34.5° N] and E5 = [19.5–22° E, 33–34.5° N]. Following Gačić et al. (2011), the averaging area has not been extended towards high levels of variability south of the Peloponnesos coast in order to avoid the noise introduced by the Pelops Gyre. The temporal evolution of the mean LF-EKE defined in boxes E1 + E2 + E3 + E4 + E5 during the period 1993–2011 is shown on Fig. 10. Its variations are almost identical to those obtained with the temporal component of the LF-EKE EOF first mode. As in Fig. 5, an horizontal level

OSD
9, 2081–2120, 2012

($22.5\,cm^2\,s^{-2}$) has been chosen that allows to differentiate phases of weak LF-EKE intensities (i.e. corresponding to the absence or to a weak activity of the MIJ) from phases of strong LF-EKE intensities (i.e. corresponding to a strong activity of the MIJ). The mean boxed LF-EKE of Fig. 10 confirms the absence or the weak activity of the MIJ during the fully "anticyclonic" period of 1993–1996, while it clearly shows an intense activity of the MIJ during both the "cyclonic-zonal" period of 1998–2005 and the "anticyclonic-zonal" period of 2006–2010.

Therefore, an oceanic indicator that would be only based on mean boxed LF-EKE would not be able to discriminate the "Cyclonic-Zonal" state period (e.g. 1998–2005) from the "Anticyclonic-Zonal" state period (e.g. 2006–2010).

5.4 The IoSC altimetry-based indicator

Thus, it is possible and necessary to combine the oceanic indicator based on mean boxed SLA with the one based on mean boxed LF-EKE in order to discriminate fully "anticyclonic" state during which the MIJ is absent (period 1993–1996) from those in which the anticyclonic NIG is able to coexist with an intense zonal MIJ (period 2006–2010). The time series of the mean standardized SLA minus the mean standardized LF-EKE as previously defined in boxes S1 (Fig. 10) and E1 + E2 + E3 + E4 + E5 (Fig. 5) respectively is shown during the period 1993–2011 (Fig. 15, red line).

Level 0 and level 1 have been mentioned on Fig. 15 in order to differentiate the 3 Ionian surface circulation phases: the "fully Anticyclonic" phases (above level 1), the "Zonal-Cyclonic" phases (under level 0) during which the cyclonic surface circulation may disappear, and the mixed "Anticyclonic-Zonal" phases (between level 0 and level 1) in which the coexistence of the two former states is possible. Transition phases also appear between level 0 and level 1, as during year 1997. Note that the downward peak occurring during year 2007 on Fig. 15 is partly due to a strong anomaly of LF-EKE as shown on Fig. 14. Yearly (Fig. 16) and monthly average ADT fields (not shown) indicate that this intense LF-EKE values are partly associated with a stationary Libyan

OSD
9, 2081–2120, 2012

mesoscale eddies, also observed in Gerin et al. (2009). This downward peak may be weakened by choosing another set of boxes, i.e. S1 and E2 + E3 + E4, that is, in a region restricted to the highest variability areas and more located to the central part of the Ionian basin (blue line on Fig. 15). During the "anticyclonic" and "zonal-cyclonic" phases, the red and blue lines of Fig. 15 are very similar, which demonstrates the robustness of the indicator. The mixed "anticyclonic-zonal" phase of years 2006 and 2007 seems to be more sensitive to boxes location, which may be due to its more unsteady nature.

Finally, the oceanic indicator of Fig. 15 reveals that the well-discussed reversals of year 1997 and 2005 are followed by another transition from "anticyclonic-zonal" mode to "cyclonic-zonal" mode, which took place in the middle of year 2010. This observation is strengthen by yearly (Fig. 16) and monthly average ADT fields (not shown). We conclude that the low-frequency changes in the IoSC do not correspond to strictly decadal oscillations.

6 Conclusion and perspectives

In this paper, new ocean state indicators have been derived from the SLTAC/DUACS altimeter dataset. They enable monitoring three well-known phenomena as the ENSO events in the Tropical Pacific, the Kuroshio Current Extension state in the North-Western Pacific and the Ionian Surface Circulation Reversal in the Mediterranean Sea. These indicators were obtained by averaging into specific boxes the altimeter Sea Level Anomaly or derived Eddy Kinetic Energy information. Except for the ENSO indicator, for which the Niño 3.4 box is used (initially defined for computing SST-based indices), the relevant boxes have been defined in order to best reproduce the Principal Component time series of the EOF variability mode corresponding to the dynamical phenomena to monitor. The indicator developed in the Kuroshio area clearly allowing the elongated states periods (1993–94, 2002–04 and 2010–11) to be distinguish from the contracted states periods (1997–2001 and 2009). The indicator developed in the Mediterranean

OSD
9, 2081–2120, 2012

Sea permits to separate the "zonal-cyclonic" state (1998–2005 and since 2011 up to now) from the "anticyclonic" state (1993–1996) usually discussed in the literature when describing the general surface circulation pattern of the Ionian Sea. In addition it allows identifying a third state in which both the anticyclonic circulation around the northern part of the basin and the strong zonal Mid Ionian jet co-exist (2008–2010).

These three indicators will now be updated at each Delayed-Time reprocessing but also all along the Near Real Time production.

In addition to providing a synthetic and operational diagnostic tool for monitoring the evolution of the ocean state at interannual to decadal time scales, these ocean indicators constitute a new way of assessing the quality of SLTAC products: the impact of every reprocessing or change in processing may now be evaluated in term of ocean state monitoring. For instance, the Kuroshio Extension indicator uses global SLTAC products but could in the future benefit from a regional dataset. This assessment is a complementary approach to the statistical calibration/validation done on both Level 2 products and external MyOcean SLTAC products.

In the future, we want to compare the Kuroshio and the Ionian Sea ocean state indicators with other available independent data (e.g. SST and surface drifter data), as done for the Oceanic Niño Index. Furthermore, we plan to extend our work to other well-known climatic phenomena like for instance the Western Tropical Indian Ocean (WTIO) and the Southeastern Tropical Indian Ocean (SETIO) indices in the Indian Ocean, which both have a clear signature in altimeter Sea Level Anomalies.

Acknowledgements. The altimeter products were produced by Ssalto/Duacs and distributed by Aviso with support from CNES. Aviso staff is gratefully acknowledged for the services provided. The authors would like to express their thanks to B. Qiu and G. Larnicol for fruitful discussions.

OSD
9, 2081–2120, 2012

References

Brachet, S.: Variabilité mésoéchelle océanique, comparaison altimétrie/modèle, PhD. Thesis, UPS-Toulouse III, 2005.

Borzelli, G. L. E., Gačić, M., Cardin, V., and Civitarese, G.: Eastern Mediterranean transient and reversal of the Ionian Sea circulation, Geophys. Res. Lett., 36, L15108, doi:10.1029/2009GL039261, 2009.

Criado-Aldeanueva, F., Del Río Vera, J., and García-Lafuente, J.: Steric and mass-induced Mediterranean sea level trends from 14 years of altimetry data, Global Planet. Change, 60, 563–575, doi:10.1016/j.gloplacha.2007.07.003, 2008.

Dibarboure, D., Pujol, M.-I., Briol, F., Le Traon, P.-Y., Larnicol, G., Picot, N., Mertz, F., and Ablain, M.: Jason-2 in DUACS: Updated System Description, First Tandem Results and Impact on Processing and Products, Marine Geodesy, 34, 214–241, EEA, The 2010 State of the Environment, doi:10.2800/5862, 2011.

Ducet, N., Le Traon, P.-Y., and Reverdin, G.: Global high-resolution mapping of ocean circulation from TOPEX/Poseidon and ERS-1 and -2, J. Geophys. Res., 105, 19477–19498, 2000.

Gačić, M., Borzelli, G. L. E., Civitarese, G., Cardin, V., and Yari, S.: Can internal processes sustain reversals of the ocean upper circulation? The Ionian Sea example, Geophys. Res. Lett., 37, L09608, doi:10.1029/2010GL043216, 2010.

Gačić, M., Civitarese, G., Borzelli, G. L. E., Kovačević, V., Poulain, P.-M., Theocharis, A., Menna, M., Catucci, A., and Zarokanellos, N.: On the relationship between the decadal oscillations of the northern Ionian Sea and the salinity distributions in the eastern Mediterranean, J. Geophys. Res., 116, C12002, doi:10.1029/2011JC007280, 2011.

Gerin, R., Poulain, P.-M., Taupier-Letage, I., Millot, C., Ben Ismail, S., and Sammari, C.: Surface circulation in the Eastern Mediterranean using drifters (2005–2007), Ocean Sci., 5, 559–574, doi:10.5194/os-5-559-2009, 2009.

Hamad, N., Millot, C., and Taupier-Letage, I.: A new hypothesis about the surface circulation in the eastern basin of the Mediterranean sea, Prog. Oceanogr., 66, 287–298, doi:10.1016/j.pocean.2005.04.002, 2005.

Kagimoto, T., Miyazawa, Y., Guo, X., and Kawajiri, H.: High resolution Kuroshio forecast system: Description and its applications, in: High Resolution Numerical Modelling of the Atmosphere and Ocean, edited by: Hamilton, K. and Ohfuchi, W., Springer New York, 209–239, 2008.

OSD
9, 2081–2120, 2012

Klein, B., Roether, W., Manca, B. B., Bregant, D., Beitzel, V., Kovacevic, V., and Luchetta, A.: The large deep water transient in the Eastern Mediterranean, Deep Sea Res. I, 46, 371–414, 1999.

Kramer, W., Dijkstra, H. A., Pierini, S., and van Leeuwen, P. J.: Measuring the impact of observations on the predictability of the Kuroshio Extension in a shallow-water model, J. Phys. Oceanogr.,42, 3–17, ISSN 0022-3670, 2011.

Larnicol, G., Ayoub, N., and Le Traon, P.-Y.: Major changes in Mediterranean Sea level variability from 7 years of TOPEX/Poseidon and ERS-1/2 data, J. Mar. Sys., 33–34, 63–89, doi:10.1016/S0924-7963(02)00053-2, 2002.

Pinardi, N., Korres, G., Lascaratos, A., Roussenov, V., and Stanev, E.: Numerical simulation of the interannual variability of the Mediterranean Sea upper ocean circulation, Geophys. Res. Lett., 24, 425–428, doi:10.1029/96GL03952, 1997.

Pujol, M.-I.: Analyse de la variabilité de surface en Méditerranée à partir des données altimétriques et comparaison aux simulations MERCATOR er MOG2D, Ph.D. thesis, UPS-Toulouse III, 2006.

Pujol, M.-I. and Larnicol, G.: Mediterranean Sea eddy kinetic energy variability from 11 years of altimetric data, J. Mar. Sys., 58, 121–142, doi:10.1016/j.jmarsys.2005.07.005, 2005.

Qiu, B.: The Kuroshio extension system: Its large-scale variability and role in the midlatitude ocean-atmosphere interaction, J. Phys. Oceanogr., 58, 57–75, 2002.

Qiu, B.: Kuroshio Extension variability and forcing of the Pacific decadal oscillations: Responses and potential feedback, J. Phys.Oceanogr., 33, 2465–2482, 2003.

Qiu, B. and Chen, S.: Variability of the Kuroshio Extension Jet, Recirculation Gyre, and Mesoscale Eddies on Decadal Time Scales, J. Phys. Oceanogr., 35, 2090–2103, 2005.

Qiu, B. and Lukas, R.: Seasonal and interannual variability of the North Equatorial Current, the Mindanao Current and the Kuroshio along the Pacific western boundary, J. Geophys. Res., 101 12315–12330, 1996.

Reynolds, R. W., Rayner, N. A., Smith, T. M., Stokes, D. C., and Wang, W.: An improved in situ and satellite SST analysis for climate, J. Clim., 15, 1609–1625, 2002.

Rio, M.-H., Poulain, P.-M., Pascal, A., Mauri, E., Larnicol, G., and Santoleri, R.: A mean dynamic topography of the Mediterranean Sea computer from altimeter data, in situ measurements and a general circulation model, J. Mar. Sys., 65, 484–508, 2007.

OSD

9, 2081–2120, 2012

Rio, M.-H., Guinehut, S., and Larnicol, G.: The New CNES-CLS09 global Mean Dynamic Topography computed from the combination of GRACE data, altimetry and in-situ measurements, J. Geophys. Res., 116, C07018, doi:10.1029/2010JC006505, 2011.
Roether, W., Klein, B., Manca, B. B., Theocharis, A., and Kioroglou, S.: Transient eastern Mediterranean deep waters in response to the massive densewater output of the Aegean Sea in the 1990's, Prog. Oceanogr., 74, 540–571, doi:10.1016/j.pocean.2007.03.001, 2007.
Smith, T. M. and Reynolds, R. W.: Improved Extended Reconstruction of SST (1854–1997), J. Clim., 17, 2466–2477, 2004.
SSALTO/DUACS users' handbook: http://www.aviso.oceanobs.com/fileadmin/documents/data/tools/hdbk_duacs.pdf, 2011.
Vigo, M. I., Garcia, D., and Chao, B. F.: Change of sea level trend in the Mediterranean and Black seas, J. Mar. Res., 63, 1085–1100, doi:10.1357/002224005775247607, 2005.
Vigo, M. I., Sánchez-Reales, J. M., Trottini, M., and Chao, B. F.: Mediterranean Sea level variations: Analysis of the satellite altimetric data, 1992–2008, J. Geodyn., 52, 271–278, doi:10.1016/j.jog.2011.02.002, 2011.

OSD
9, 2081–2120, 2012

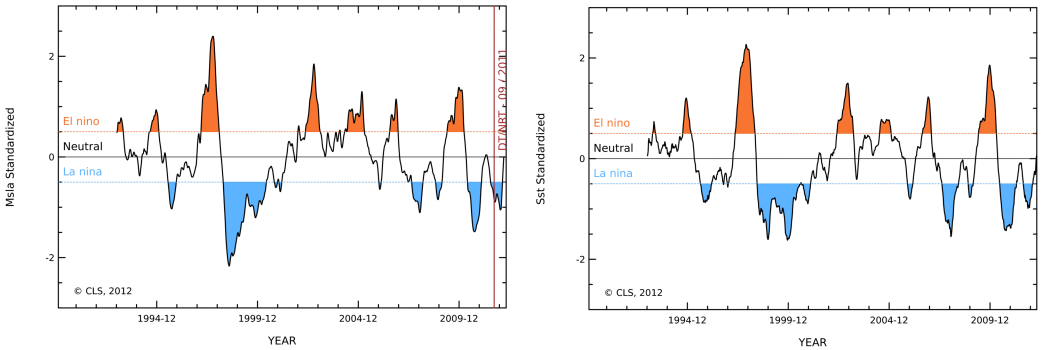

Fig. 1. Time series of SLA (left) and SST (right) divided by the respective standard deviation over the area and referenced to the 1993–2006 base period. In blue are la Niña events, in red el Niño.

OSD
9, 2081–2120, 2012

Ocean state indicators from MyOcean altimeter products

L. Bessières et al.

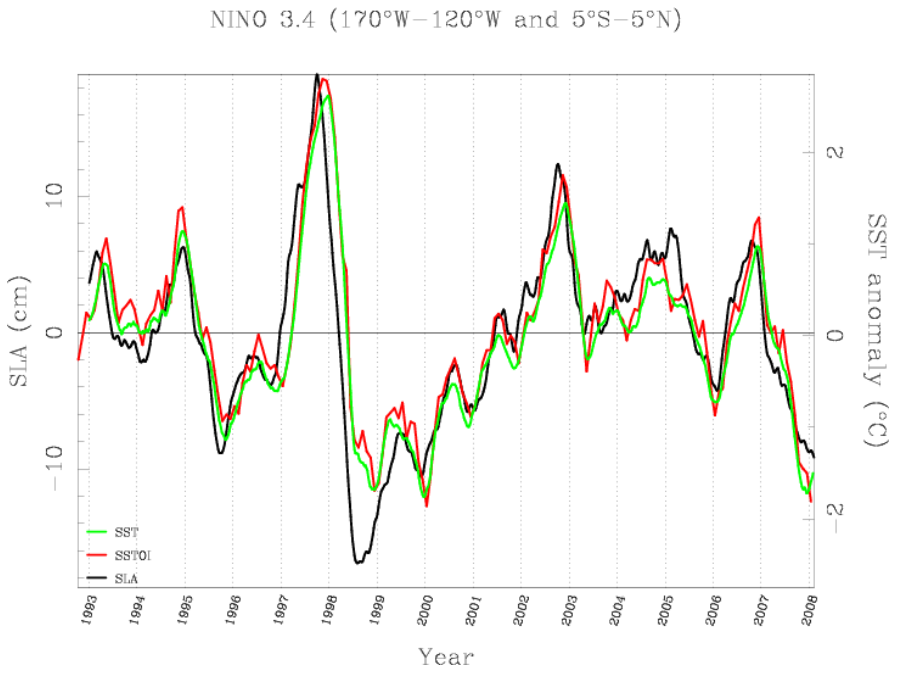

Fig. 2. Time evolution of SLA in black referenced the 1993–2006 base period. In green the SST anomaly from Reynolds fields also referenced to the 1993–2006 base period and in red, the SST anomaly from NOAA ERSST.v2 SST fields referenced to the 1971–2000 base period. The latter is plotted from the ascii file obtained at: ftp://ftp.cpc.ncep.noaa.gov/wd52dg/data/indices.

OSD
9, 2081–2120, 2012

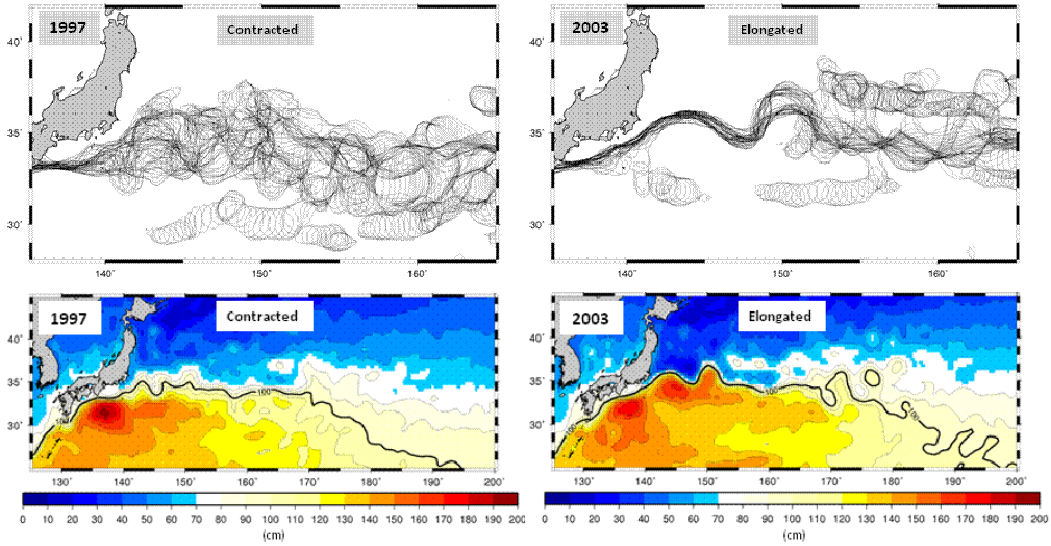

Fig. 3. (Upper panels) Yearly paths defined by the 100-cm contours in the weekly ADT fields for the 1997 contracted state (left) and the 2003 elongated state (right). (Lower panels) Yearly averaged ADT with a 10 cm contour interval and a thick line denoting 100 cm in the KE region during year 1997 (left) and year 2003 (right).

OSD
9, 2081–2120, 2012

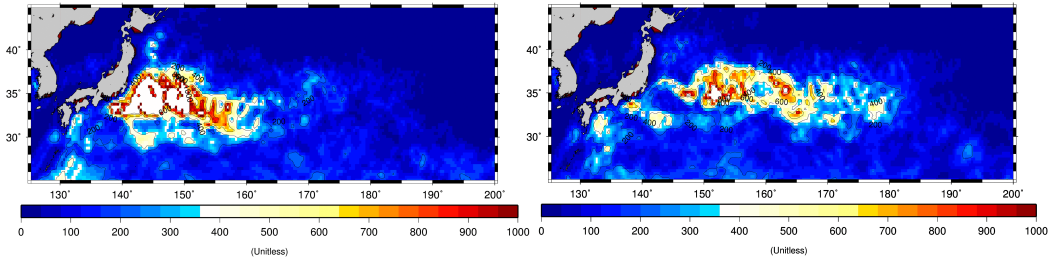

Fig. 4. Yearly averaged high-frequency EKE in the KE region, during the 1997 contracted state (left panel) and the 2003 elongated state (right panel).

OSD
9, 2081–2120, 2012

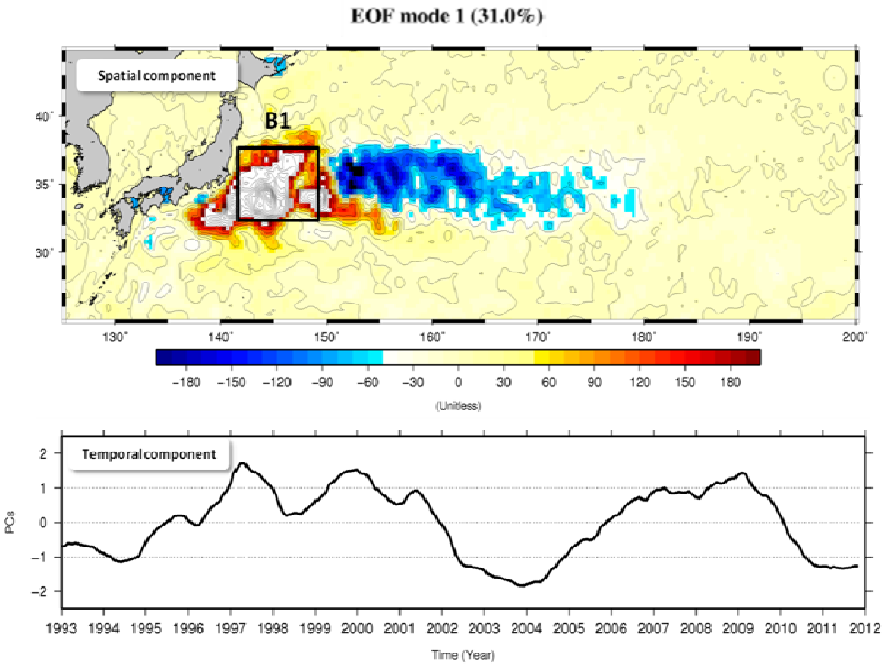

Fig. 5. Mode 1 spatial distribution of the 1993–2011 mean high-frequency EKE EOF decomposition in the KE region (upper panel) and its associated temporal component (lower panel). The box B1 is localized between 142–149° E and 32–37° N on top panel for later purpose.

OSD
9, 2081–2120, 2012

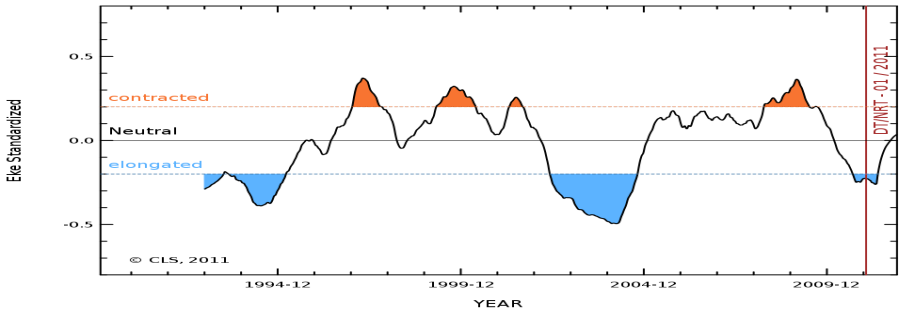

Fig. 6. Mean standardized HF-EKE defined in box B1 in the KE region, during the period 1993–30 November 2011 (see Fig. 5 for B1 spatial location). Blue shaded areas correspond to elongated states periods, while orange shaded areas fit contracted states periods. The vertical red line indicates the transition between the delayed time (DT) and the near real time (NRT) production modes of the SLA used for the HF-EKE calculation.

OSD
9, 2081–2120, 2012

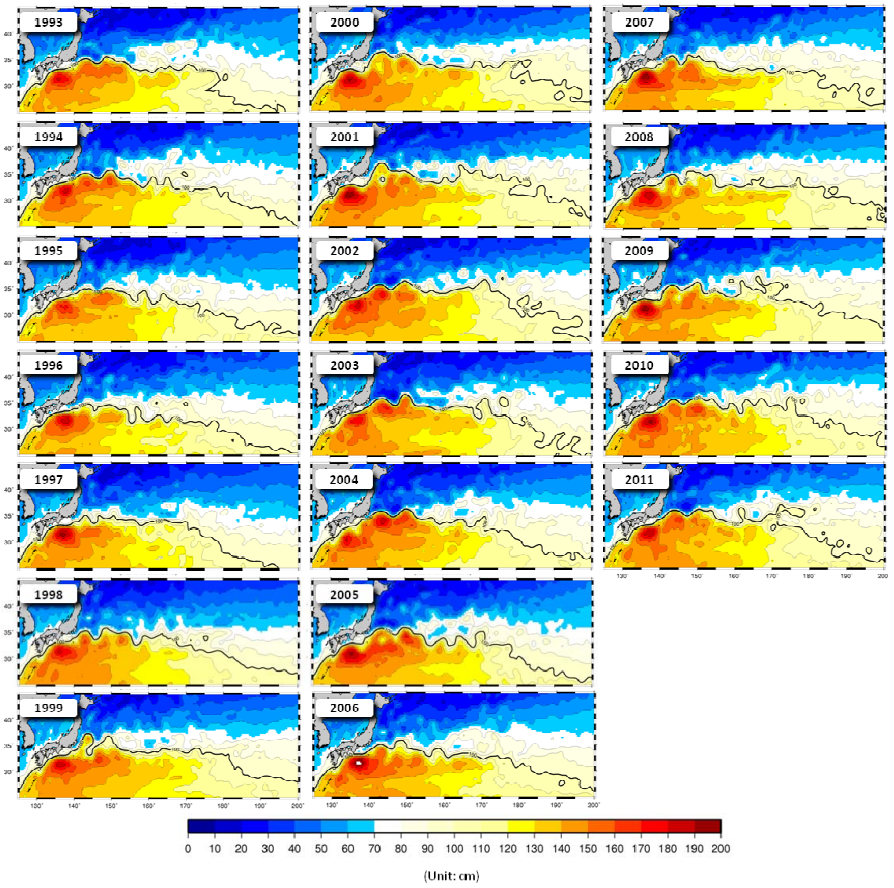

Fig. 7. Yearly averaged ADT with a 10 cm contour interval and a thick line denoting 100 cm in the KE region from year 1993 (upper left panel) to year 2011 (lower right panel). Data of the near real time (NRT) production mode are used during year 2011, from 26 January to 30 November. Unit in cm.

OSD
9, 2081–2120, 2012

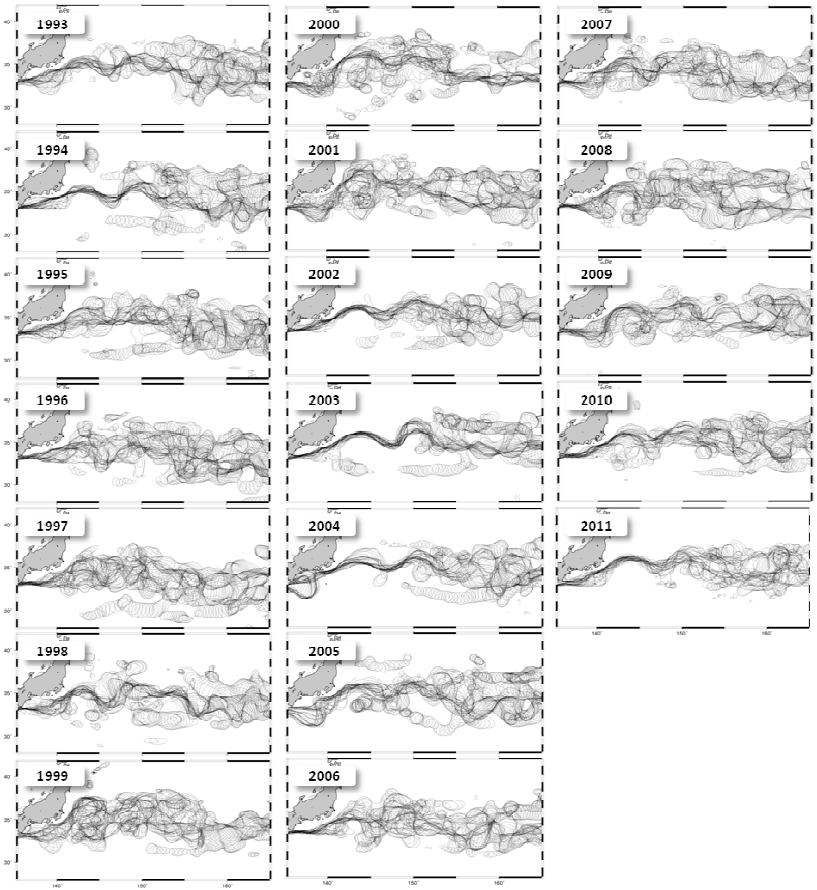

Fig. 8. Yearly path defined by the 100-cm contours in the weekly ADT fields in the KE region from year 1993 (upper left panel) to year 2011 (lower right panel). Data of the near real time (NRT) production mode are used during year 2011, from 26 January to 30 November.

OSD
9, 2081–2120, 2012

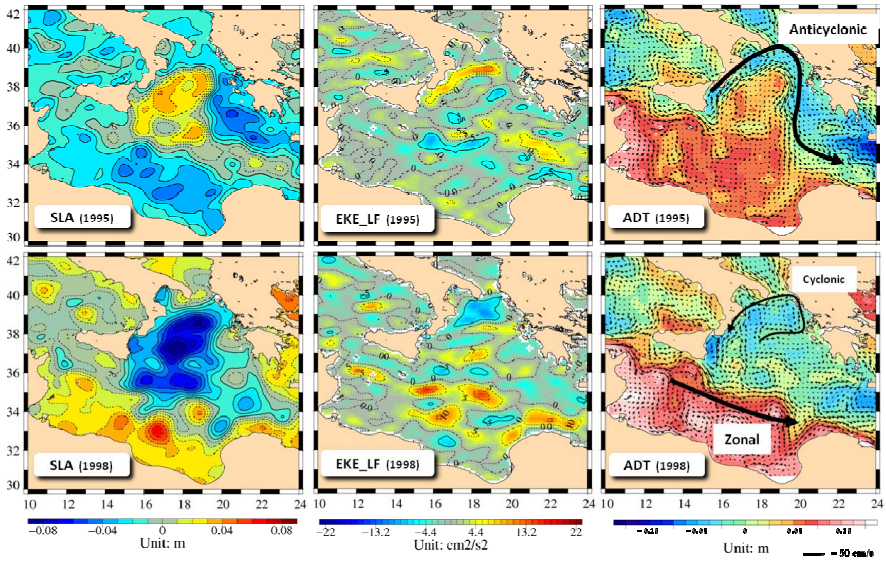

Fig. 9. Yearly averaged SLA, EKE_LF and ADT with overlaid total velocity field (resp. left, middle and right panels) in the Ionian region during year 1995 (top panels) and year 1998 (bottom panels). Units respectively in m, $cm^2\,s^{-2}$ and m. Vector field scale: 50 $cm\,s^{-1}$.

OSD
9, 2081–2120, 2012

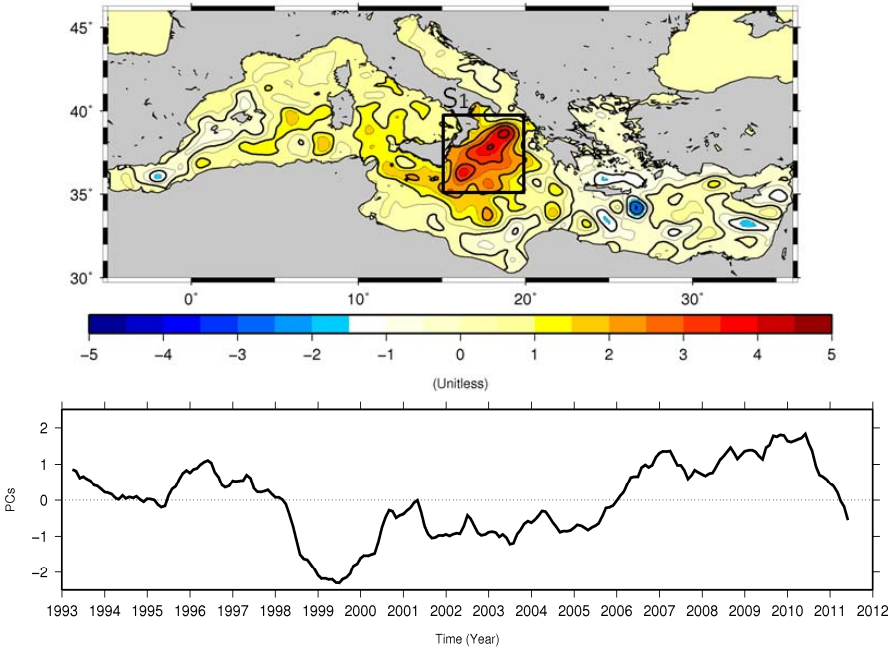

Fig. 10. Mode 2 spatial distribution of the 1993–2011 mean SLA EOF decomposition in the Mediterranean Sea (top panel) and its associated temporal component (bottom panel). This mode explains 14.0 % of the total variance. The box S1 is localized between 15–20° E and 35–40° N on top panel.

OSD
9, 2081–2120, 2012

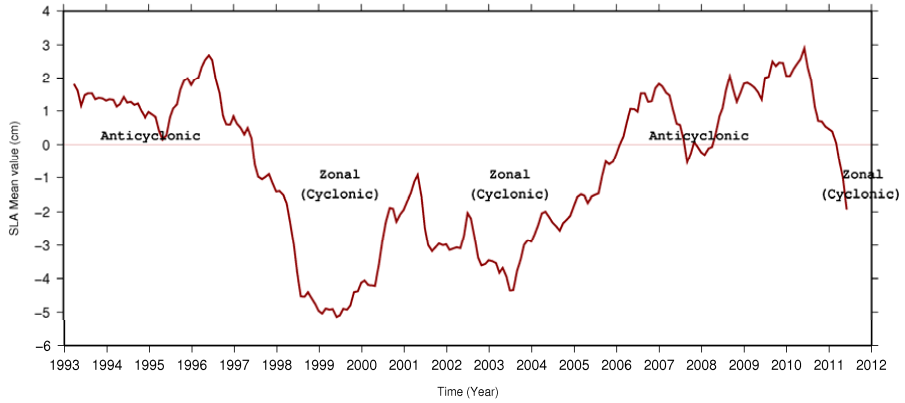

Fig. 11. Time series in the Ionian region during the period 1993–2011 of mean SLA in box S1 as defined in Fig. 10 (top panel), units in cm. The red level has been mentioned in order to differentiate the NIG phases: the "Anticyclonic" phases (above red level), the "Cyclonic" phases (under red level).

OSD
9, 2081–2120, 2012

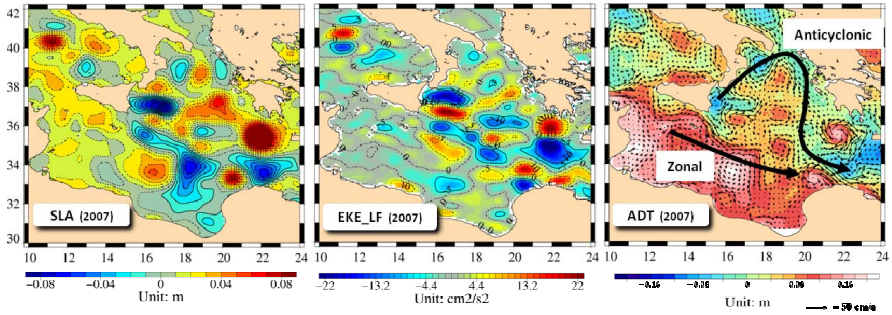

Fig. 12. Yearly averaged SLA, centered EKE_LF and ADT with overlaid total velocity field (resp. left, middle and right panels) in the Ionian region during year 2007. Units respectively in m, $cm^2\ s^{-2}$ and m. Vector field scale: 50 $cm\ s^{-1}$.

OSD
9, 2081–2120, 2012

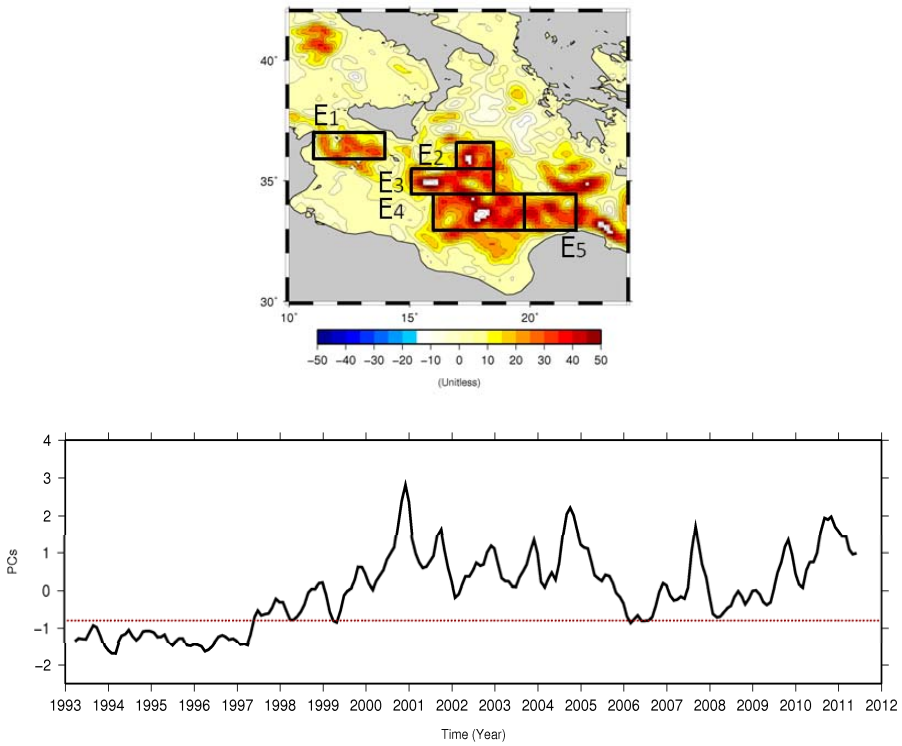

Fig. 13. Mode 1 spatial distribution of the 1993–2011 mean low-frequency EKE EOF decomposition in the Ionian region (Top panel) and its associated temporal component (bottom panel). This mode explains 12.0 % of the total variance. The level corresponding to −0.9 has been mentioned in order to differentiate phases of weak/strong LF-EKE intensities in relation with the absence/presence of the MIJ respectively. Five boxes are localized on top panel: E1 = [11–14° E, 36–37° N], E2 = [17–18.5° E, 35.5–36.5° N], E3 = [15–18.5° E, 34.5–35.5° N], E4 = [16–19.5° E, 33–34.5° N] and E5 = [19.5–22° E, 33–34.5° N].

OSD
9, 2081–2120, 2012

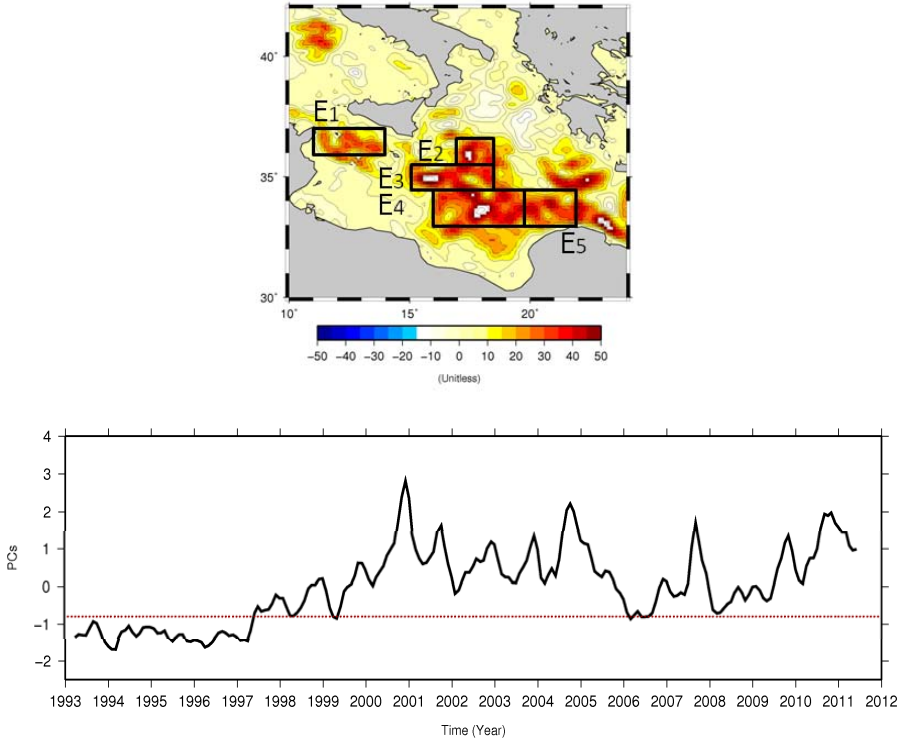

Fig. 14. Time series of mean LF-EKE in boxes E1 + E2 + E3 + E4 + E5 as defined in Fig. 13 during the period 1993–2011. Units in $cm^2\ s^{-2}$.

OSD
9, 2081–2120, 2012

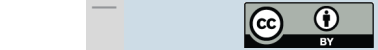

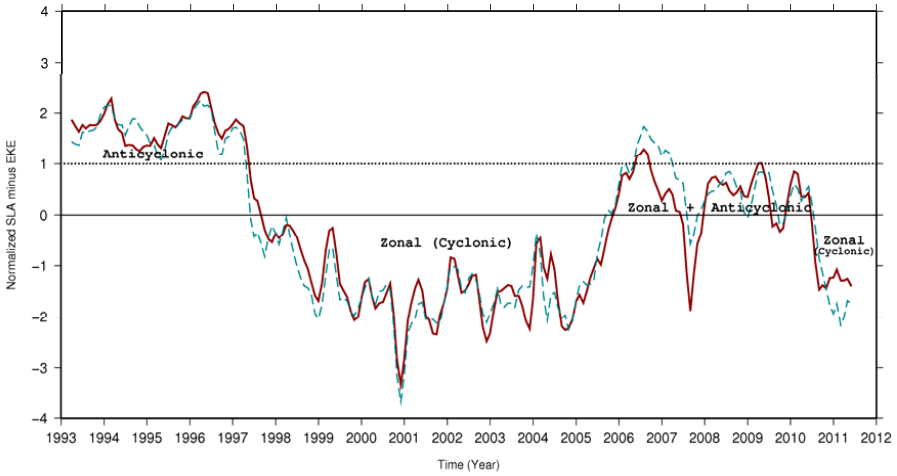

Fig. 15. Time series of mean standardized SLA minus mean standardized LF-EKE in previously defined respective boxes in the Ionian region during the period 1993–2011: average in boxes S1 and E1 + E2 + E3 + E4 + E5 (red line) and average in S1 and E2 + E3 + E4 (blue dashed line). Level 0 and level 1 have been mentioned in order to differentiate surface circulation phases.

OSD
9, 2081–2120, 2012

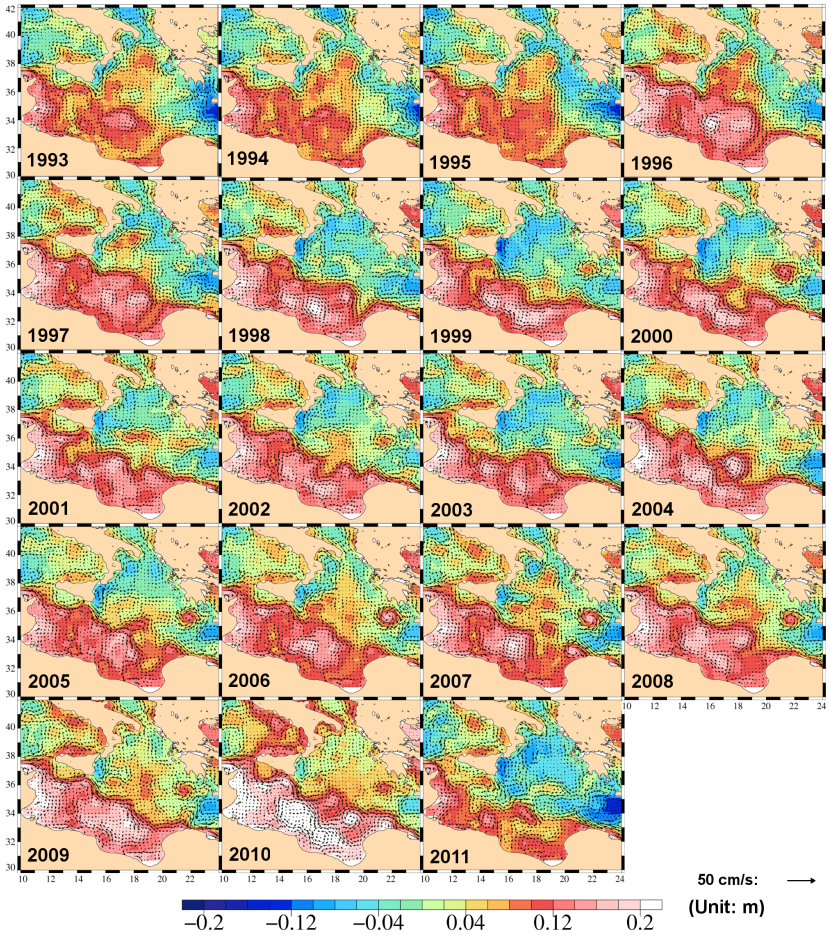

Fig. 16. Yearly averaged ADT with overlaid total velocity field in the Ionian region from year 1993 (upper left panel) to year 2011 (lower left panel). Unit in m, vector field scale: 50 cm s^{-1}.

OSD
9, 2081–2120, 2012